Supplemental Material of "Computational acceleration of prospective dopant discovery in cuprous iodide"

Miglė Graužinytė, Silvana Botti, Miguel A. L. Marques, Stefan Goedecker and José A. Flores-Livas

June 28, 2019

Reference phase data

The information on the chemical reference phase data used to calculate the formation energies provided in the main article is summarized in Table 1 and Table 2. This information includes the space group of the crystalline phase, its materials project ID number and formation energies (evaluated per formula unit) calculated using the relevant exchange-correlation functionals.

Table 1: List of the elemental phases used in the formation energy calculations

Defect atom	Spg	MPID	E^{PBE} (eV)	E^{PBE0} (eV)
Cu	$Fm\bar{3}m$	**mp-30**	-3.729	-3.854
I	$Ccme$	**mp-23153**	-1.518	-2.345
O	-	-	-4.937	-6.937
S	$P2/c$	**mp-96**	-4.128	-5.575
Se	$P3_121$	**mp-14**	-3.499	-4.940
Te	$P3_121$	**mp-19**	-3.142	-4.462
Po	$P3_121$	N/A	-3.082	-4.287
Be	$P6_3/mmc$	**mp-87**	-3.773	-3.881
Mg	$P6_3/mmc$	**mp-153**	-1.504	-1.510
Ca	$P6_3/mmc$	**mp-132**	-1.918	-1.800
Sr	$Fm\bar{3}m$	**mp-76**	-1.639	-1.589
Ba	$Im\bar{3}m$	**mp-122**	-1.909	-1.783
Ra	$Im\bar{3}m$	N/A	-1.322	-1.260
Sn	$Fd\bar{3}m$	**mp-117**	-3.846	-5.012
Pb	$Fm\bar{3}m$	**mp-20483**	-3.570	-4.480

Solid elemental phases were used as a reference for all atomic species with the exception of oxygen, where we considered an isolated O_2 molecule in a large box of $10\times10\times10$ Å^3. Calculation parameters and convergence criteria analogous to those presented in the main body of the article were used to perform reference phase calculations. Here, k-point meshes had to be adjusted for each elemental phase and were

chosen such that changes in energy no larger than 1-3 meV/atom result. The same PAW files were used for the reference phase and defective supercell calculations. Note that all reference phase structures were relaxed with the parameters indicated above and may, therefore, deviate slightly from those found in the materials project database.

A handful of low energy structures of Cu_mD_n and D_kI_l compounds were considered to address secondary phase formation between the defect species and the host atoms. No ternary compound formation was considered in this work. The phases found to create the tightest chemical potential bounds (under Cu-rich conditions reported in the main article) are presented in Table 2 for each impurity species.

Table 2: List of the secondary phases used in the formation energy calculations

Defect atom	Formula	Spg	MPID	E^{PBE} (eV)	E^{PBE0} (eV)
O	CuO	$P4_2/mmc$	**mp-1692**	-1.195	-1.410
S	CuS_2	$Pnnm$	**mp-849086**	-0.311	-0.539
Se	$CuSe_2$	$Pnnm$	**mp-2000**	-0.279	-0.212
Te	CuTe	$Pmmn$	**mp-20826**	-0.146	-0.263
Be	BeI_2	$Imcb$	**mp-570886**	-1.736	-2.087
Mg	MgI_2	$P\bar{3}m1$	**mp-23205**	-3.199	-3.864
Ca	CaI_2	$P\bar{3}m1$	**mp-30031**	-4.955	-5.529
Sr	SrI_2	$Pnma$	**mp-568284**	-5.140	-5.755
Ba	BaI_2	$Pnma$	**mp-569619**	-5.397	-6.109
Ra	RaI_2	$Pnma$	N/A	-5.342	-6.066
Sn	SnI_2	$C2/m$	**mp-27194**	-1.498	-1.572
Pb	PbI_2	$R\bar{3}m$	**mp-22883**	-2.040	-2.280

The chemical potential reference does not alter the position of the thermodynamic transition (ionization) levels of individual defects. Thus, the assessment of a defect as shallow or deep is not altered by the inclusion of the chemical potential. As a result, and to minimize the computational costs, detailed reference phase information was only checked for impurities identified as prospective dopants. In those cases, other quantities, such as the relative concentration of impurity defects vs. native defects (for example the copper vacancy), become important and the chemical potential plays a significant role.

Pseudopotentials

The PAW pseudopotentials used to investigate impurity defects in γ-CuI are listed in Table 3: the date identifying the PAW and the number of electrons considered as valence used for each atomic species are reported. Due to the high-throughput nature of the study, the computationally lightest PAWs available were chosen for most atomic species. Additional validation tests of the PAWs chosen were performed for the elements highlighted in bold (those that were identified as potential n-type or p-type dopants in the main article), showing no strong changes in the thermodynamic transition (ionization) levels reported, as summarized in the following section.

Table 3: Information on the PAW files used for performing defect calculations in γ-CuI. The number of valence electrons and the PAW identifying date is indicated. The elements that were identified as potential dopants are highlighted in bold.

Atomic species	PAW type	No. elec.	Atomic species	PAW type	No. elec.
Ag	02Apr2005	11	Na	08Apr2002	1
Al	04Jan2001	3	Nb	08Apr2002 (pv)	11
As	22Sep2009	5	Ni	02Aug2007	10
Au	04Oct2007	11	**O**	**08Apr2002**	**6**
B	06Sep2000	3	Os	17Jan2003	8
Ba	**06Sep2000 (sv)**	**10**	P	06Sep2000	5
Be	**06Sep2000**	**2**	**Pb**	**08Apr2002**	**4**
Bi	08Apr2002	5	Pd	04Jan2005	10
Br	06Sep2000	7	**Po**	**10Feb2004**	**6**
C	08Apr2002	4	Pt	04Feb2005	10
Ca	**06Sep2000 (pv)**	**8**	**Ra**	**29May2007 (sv)**	**10**
Cd	06Sep2000	12	Rb	06Sep2000 (pv)	7
Cl	06Sep2000	7	Re	17Jan2003	7
Co	02Aug2007	9	Rh	04Feb2005	9
Cr	06Sep2000	6	Ru	04Feb2005	8
Cs	08Apr2002 (sv)	9	**S**	**06Sep2000**	**6**
F	08Apr2002	7	Sb	06Sep2000	5
Fe	06Sep2000	8	Sc	04Feb2005	3
Fr	29May2007 (sv)	9	**Se**	**06Sep2000**	**6**
Ga	08Apr2002	3	Si	05Jan2001	4
Ge	05Jan2001	4	**Sn**	**06Sep2000 (d)**	**14**
H	06Feb2004 (h)	1	**Sr**	**07Sep2000 (sv)**	**10**
Hf	20Jan2003	4	Ta	17Jan2003	5
Hg	06Sep2000	12	Tc	04Feb2005	7
In	08Apr2002	3	**Te**	**08Apr2002**	**6**
Ir	06Sep2000	9	Ti	08Apr2002	4
K	17Jan2003 (pv)	7	Tl	08Apr2002	3
Li	17Jan2003	1	V	08Apr2002	5
Mg	**13Apr2007**	**2**	W	08Apr2002	6
Mn	06Sep2000	7	Y	25May2007 (sv)	11
Mo	08Apr2002	6	Zn	06Sep2000	12
N	08Apr2002	5	Zr	04Jan2005 (sv)	12

Validation tests

Unit cell

Energy cut-off and k-point convergence tests were performed for the conventional unit cell of γ cuprous iodide. Figure 1 summarizes the results. It is clear that the excellent convergence of <1 meV/atom is reached for a Γ-mesh of 6×6×6 and ENCUT=700 used in the production calculations. A 3×3×3 Γ-mesh in a 2×2×2 supercell is equivalent to the 6×6×6 mesh in the conventional cell.

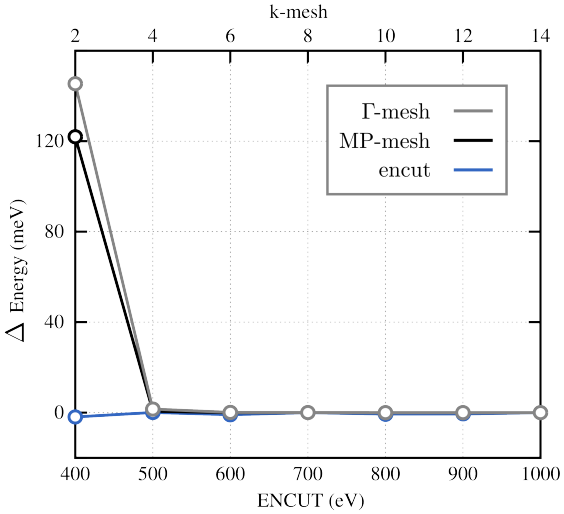

Figure 1: Convergence tests performed in the conventional cell of γ-CuI. Differences in total energy of the cell (6 atoms) are reported with respect to the highest parameter value tested (ENCUT = 1000 eV and k-point mesh of 14×14×14). Chemical accuracy (<1 meV/atom) is already achieved at ENCUT = 400 eV and k-point meshes of 4×4×4 irrespective of the centering.

Valence electrons

For all impurity elements identified as important defects in the host CuI lattice (highlighted in bold in Table 3) we considered PAWs with more valence electrons. Among these elements, PAWs with an increased number of valence electrons were found to be available for only five atomic species: four n-type elements (Be, Mg, Ca and Pb) and one p-type element (Po). GW or high-pressure pseudopotentials were not considered.

Table 4: The effects of PAWs with a higher number of valence electrons. ΔE marks the total energy increase of the defective supercell for the relevant charge state q. $\Delta\epsilon$ marks the change in the thermodynamic transition energy between the charge states. The increase in the number valence electrons is also indicated in parenthesis.

Defect type	charge(q)	ΔE (meV)	$\Delta\epsilon$ (meV)
Be_{Cu}	0	1	
$(2 \rightarrow 4)$	+1	8	7
Mg_{Cu}	0	-11	
$(4 \rightarrow 10)$	+1	-10	1
Ca_{Cu}	0	1	
$(8 \rightarrow 10)$	+1	7	6
Pb_{Cu}	0	4	
$(4 \rightarrow 14)$	+1	-20	-24
Po_{I}	0	-6	
$(6 \rightarrow 16)$	-1	-10	-4

The effect of the choice of the pseudopotential on the reported formation energies and transition levels was checked using the PBE level of theory. The results are summarized in Table 4. The effect of the PAW was found to be negligible for all elements, with the largest change (-24 meV) in the thermodynamic transition level observed for the Pb_{Cu} defect upon the introduction of *d*-shell electrons into the valence. The negative sign indicating that the transition level becomes shallower with increasing number of valence electrons. To confirm that this effect is not larger for hybrid functionals, the PAWs were also checked using PBE0 for the Pb_{Cu} defect. While the change in the formation energy of each individual charge state increased to almost -45 meV using hybrid functionals, it affected both charge states similarly, resulting in largely unchanged ionization level, with $\Delta\epsilon_{PBE0}$ of only 12 meV.

Size of the supercell

The supercell size convergence was checked using the PBE level of theory, by comparing the formation energies between a 2×2×2 (64 atoms) and a 3×3×3 (216 atoms) sized supercell for a selection of defects. We considered the copper vacancy, V_{Cu}, representing a shallow acceptor defect, an iodine vacancy, V_I, representing a deep amphoteric defect, and a magnesium substitutional, Mg_{Cu}, representing (the lowest energy) shallow electron donor. The results are summarized in Table 5.

Table 5: ΔE denotes the increase in the total formation energy in a 3×3×3 defective supercell (when compared to a 2×2×2 supercell) and $\Delta\epsilon$ is the change in the transition energy between the two charge states reported.

Defect type	charge(q)	ΔE (meV)	$\Delta\epsilon$ (meV)
V_{Cu}	0	31	
V_{Cu}	-1	-6	-37
V_I	+1	-2	
V_I	-1	-100	-98
Mg_{Cu}	0	-60	
Mg_{Cu}	+1	-20	40

We note that for the ionized states of the shallow defects we observe an excellent agreement between the larger and smaller supercell results, with poorer accuracy for charge neutral states of the same defects. Nevertheless, the total shifts in the thermodynamic transition levels (consistently favoring p-type conductivity) are small enough not to affect the conclusions of the main article. The largest dependence with the supercell size is observed for the deep defect, V_I. However, due to the amphoteric nature of the defect, the 0.1 eV shift would not impact significantly the p-type or n-type conductivity in γ-CuI.

Effect of PBE0 structural relaxations

All hybrid-functional defect-related properties reported in the main article were calculated by compressing the relaxed PBE atomic geometry to the PBE0 predicted lattice size. To confirm the validity of this approach we investigated the effect of local atomic relaxations using the PBE0 functional for a small subset of defects. A Monkhorst-Pack centered 2×2×2 k-point mesh was used to perform the relaxations, while a 3×3×3 Γ-point mesh was used to obtain the final energy of the supercell. The results are summarized in Table 6. The total change in the supercell energy upon relaxation $\Delta E = E_{\text{relax}} - E_{\text{fixed}}$ is reported together with the change in the bond lengths between the defect atom, D, and its nearest neighbor, $\Delta d^{\text{D-I/Cu}} = d_{relax}^{\text{D-I/Cu}} - d_{fixed}^{\text{D-I/Cu}}$. For the case of the native Cu vacancy, the latter is challenging

to evaluate, however Table 6 reveals that the total energies are virtually unchanged by the PBE0 atomic relaxation surrounding this defect.

Table 6: Summary of the effects of the local atomic relaxation using the PBE0 functional for a selection of defects. ΔE is the energy change following the atomic relaxations. Δ $\mathrm{d}^{\mathrm{D-I/Cu}}$ is the change in the bond distances between the defect D and the surrounding I or Cu atoms.

Defect type	charge(q)	ΔE (meV)	$\Delta d^{\mathrm{D-I/Cu}}$ (pm)
V_{Cu}	0	-4.6	–
V_{Cu}	-1	+1.3	–
Be_{Cu}	-1	+0.6	-14.97
Be_{Cu}	0	-5.4	-18.57
Be_{Cu}	+1	-8.7	-23.39
O_I	-1	-1.3	-3.07
O_I	0	+2.8	-8.34
O_I	+1	-1.7	-8.25

In all three cases considered — V_{Cu} (representing a native defect), O_I (representing p-type dopants) and Be_{Cu} (representing n-type dopants) — changes in the total energy of around 10 meV were observed. Similarly, the changes in bonding distances were measured in pm, with the largest relaxation of 24 pm found for the donor charge state of Be_{Cu}. This small impact of the atomic relaxations could have been anticipated: (i) the change in the lattice between PBE0 and PBE predictions is very small ($< 0.05\%$); (ii) we are explicitly interested in shallow donors/acceptors. The nature of these defects indicates bulk-derived occupied bands, to which the defect atom (and hence atomic relaxations around it) do not contribute strongly.

In contrast, localized occupied defect-atom-derived states, such as in the case of Sn_{Cu} and Pb_{Cu} (see Figure 6 in the main article), could be more significantly affected by atomic PBE0 relaxations. However, the localized nature of these defects makes them ineffective dopants rendering, as such, the effect of local relaxations of no further interest for our investigation.

Defect concentrations under unfavorable conditions

In Figure 3 and Figure 5 of the main article, we report impurity defect concentrations in thermodynamic equilibrium under the conditions (Cu-rich) that are most favorable for defect incorporation. Here, we present the analogous plot of defect concentrations in CuI under Cu-poor conditions for comparison.

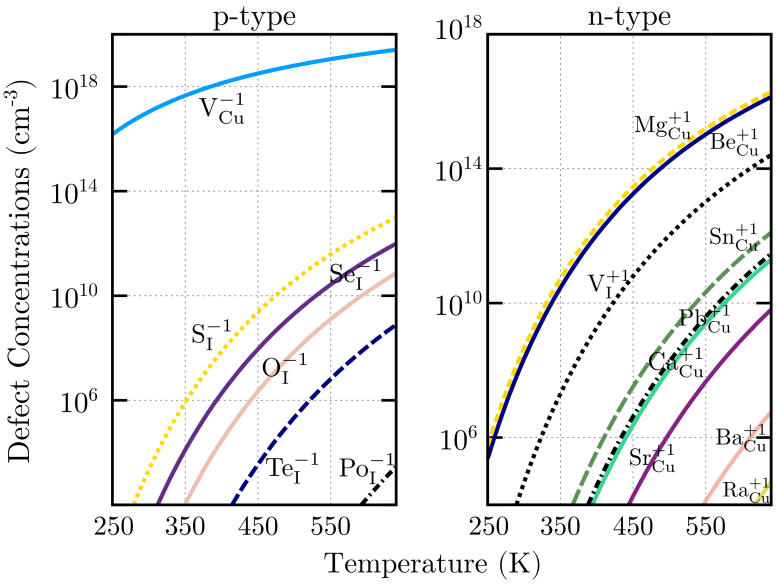

Figure 2: Left panel: PBE0 formation energies of potential p-type dopants, as well as the native V_{Cu}, evaluated at Cu-rich conditions. Only the stable charge states are shown. Right panel: Calculated charged defect concentrations in thermal equilibrium (using Boltzmann statistics), based on the formation energies shown in the left panel.